

NUMERICAL INVESTIGATION OF THE RESOLUTION IN SOLID IMMERSION LENS SYSTEMS

J. Bischoff* and R. Brunner
Carl Zeiss Jena GmbH

Carl-Zeiss-Promenade 10, 07745 Jena / Germany

ABSTRACT

Solid immersion microscopy, an optical method with the capability for superresolution has received a considerable amount of attention in the literature in the past few years. The main targets of the technique are lithography, pattern inspection (including critical dimension measurement) and data storage. The classical theory predicts a resolution gain proportional to the refraction index of the solid immersion lens. The intent of the paper is to prove this prediction by means of simulations and to find optimum measuring conditions. To this end, we present a very efficient, rigorous modeling method. By means of this method, we show that the inclusion of evanescent waves is crucial for the resolution gain. This is detailed with different excitation and detection schemes. Furthermore, we investigate the impact of polarization and different sample types.

1. INTRODUCTION

The demand for improved optical resolution is rapidly increasing due to the continuing challenges encountered in lithography, data storage and optical imaging. Much progress has been achieved in the last decade by the introduction of techniques using evanescent-fields and near-field interaction for resolution enhancement. In particular, the use of solid immersion lenses (SILs) has attracted much attention due to the additional advantages of high transmission or reflection efficiency and fast imaging^{1,2,3}. In this technique, a conventional far-field optical system is combined with a high refractive index lens (SIL) placed less than a wavelength away from the sample of interest. The diffraction-limited spot size is reduced in proportion to the index of the SIL. Usually the SIL is either a simple hemisphere or an aplanatic hyper-hemisphere, but other designs are not excluded.

A theoretical investigation is crucial for designing a SIL and for interpreting the images that are obtained. The theoretical aspects of SIL-systems have been considered in several recent papers. Ichimura et al.⁵ calculated the point spread function as a function of the air gap. Numerical approximations for spot size and a calculation of the electromagnetic field inside a multilayer system are described by Feng Guo et al.⁴ and by Milster et al.⁶. In these calculations the thin-film layers have no structure in the lateral direction. The imaging of a simple periodic metallic or dielectric multilayer grating was examined by Wei-Hung Yeh et al.⁷.

In this work, we simulate the scanning of a focussed and linearly polarized beam above nanometer-sized metal or dielectric structures. Both reflection and transmission are considered. Because our method is not restricted to homogeneous or simple lateral periodic structures, we are able to investigate a wide variety of different geometries and media. The simulations show that the interaction between propagating and evanescent fields and the sample is strongly dependent on the geometry of the sample, the material parameters, and the size of the air gap. In addition, the theoretical predictions show the importance of choosing the optimal excitation and detection geometry.

Keywords: Solid immersion microscopy, superresolution, optical modeling, optical data storage, lithography, evanescent fields, RCWA

2. THEORY

2.1 Fundamental

In the following, we describe a model for simulating scanning solid immersion microscopy of an arbitrary sample. Due to the required accuracy, a rigorous full vector treatment is necessary. The FDTD (finite difference time domain)⁸ and MMP (multiple multipole)⁹ methods are often used, however, they require a full electromagnetic computation for every scan position. As will be shown here, a frequency domain method (i.e., a modal method) in combination with the angular spectrum representation of the incident field is more efficient, even for samples with an arbitrary pattern

In order to calculate the diffracted field, the incident (focussed) electromagnetic field has to be convolved with the diffraction response of the scatterer. According to Fourier analysis, a convolution in real space is equivalent to a simple multiplication in the frequency domain. Fourier transforming the incident field yields the angular spectrum which represents an arbitrary wavefront as a superposition of plane waves with complex amplitudes $\tilde{\mathbf{A}}_m$. The angular discretization of the spectrum is governed by the ratio between spatial pitch d and wavelength via the Bloch theorem:

$$\beta_m = \beta_0 + m \frac{\lambda}{d} \quad (1)$$

with $\beta_0 = n \cdot \sin(\theta)$ (where n is the refractive index and θ the main angle of incidence) and m being the order of the Rayleigh mode. The incident spectrum can be represented by a column vector:

$$\mathbf{I} = \begin{pmatrix} \dots \\ \tilde{\mathbf{A}}_m \\ \dots \end{pmatrix}. \quad (2)$$

The response of the scatterer can be computed by a modal diffraction method (see subsection 2.2). This yields an excitation independent reflection matrix $\mathbf{R} = (r)_{o,i}$ or a transmission matrix $\mathbf{T} = (t)_{o,i}$. The product $\mathbf{R}\mathbf{I}$ (or $\mathbf{T}\mathbf{I}$) gives the angular spectrum of the diffracted wave. The angular spectrum is equivalent to the directional distribution of the diffracted light in the far field of the sample. Incidentally, the angular spectrum of the diffracted wave can be Fourier-inverted to give the spatial distribution of light in the near field.

In almost the same manner as the illumination, the detection is also focussed by means of a detector optics which relays the diffracted spectrum to a detector. The detection process is described mathematically by a row vector \mathbf{D} containing complex-valued elements D_m . Each element represents the detection efficiency in one angular direction. Of course, the same discretization has to be chosen for illumination, diffraction, and detection. The most common detector function would be a conical or annular aperture. More sophisticated detector functions could also include phase shifting units. Finally, the intensity I_D measured at the detector is proportional to squared modulus of the vector-matrix-vector product:

$$I_D \propto \left| \left(\dots \ D_m \ \dots \right)_o \cdot (r)_{o,i} \cdot \begin{pmatrix} \dots \\ \tilde{\mathbf{A}}_m \\ \dots \end{pmatrix}_i \right| \quad (3)$$

2.2 Rigorous Coupled Wave Analysis (RCWA)

Basically, the RCWA belongs to the modal methods with Fourier expansion (MMFE). “Modal” indicates that each cartesian component of the electromagnetic field is developed in terms of the transversal wavenumber component β :

$$E(z, \vec{r}) = \sum_{\vec{\beta}} E(z, \vec{\beta}) \cdot \exp(i\vec{\beta}\vec{r}) \quad (4)$$

where z is the normal direction and \vec{r} is a vector in the transversal plane. In addition, the RCWA is a modular method, i.e., the diffraction problem is solved for simple objects and then the elementary solutions are coupled by means of an appropriate matrix. The basic elements of the RCWA are slices (as sketched in fig. 1). These are flat layers (with plain interfaces) with changes of the permittivity ϵ permitted only in the transversal direction. In a modal method such as ours, the reciprocal space (or k -space) representation of ϵ is used. Then, starting from Maxwell's equations in modal notation and eliminating the normal components of the electromagnetic field, a system of second order differential equations with constant coefficients can be obtained for the transversal field components E_x , E_y , H_x and H_y . The system can then be solved by diagonalizing its characteristic matrix. This leads to matrices that describe the propagation of the Bragg-modes within a RCWA-slice and the coupling between these modes and the transversal field components at each interface between the slices. Eventually, the matrices have to be coupled to connect the cause and effect. Here, a recursive coupling scheme is strongly recommended to ensure rapid convergence of the algorithm. In the end, one obtains matrices r^f , r^b , t^f and t^b that describe the coupling between all incident cause and diffracted effect modes.

$$\begin{pmatrix} s_-^f \\ s_+^b \end{pmatrix} = \begin{pmatrix} r^f & t^b \\ t^f & r^b \end{pmatrix} \cdot \begin{pmatrix} s_+^f \\ s_-^b \end{pmatrix} \quad (5)$$

The diffraction modes in the substrate and superstrate, i.e., s_{\pm} are also called Rayleigh modes. For example, if the system (stack) is excited from the front side (s_+^f) and the detection is in reflection (s_-^f) then the diffraction is described by r^f . The submatrices r^f , r^b , t^f and t^b are dense matrices (they become diagonal for unpatterned flat layers). In case of plane wave incidence, only one column of the diffraction matrix is projected whereas a strongly focussed wave projects the whole matrix. The cause and effect modes are depicted schematically in fig. 1.

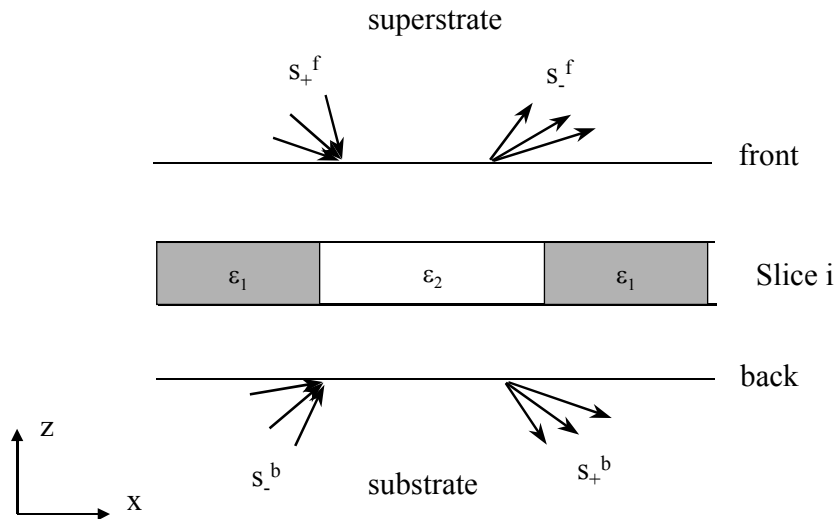


Fig. 1: Scheme of a patterned multilayer stack. The stack comprises RCWA-slices (e.g., slice i) as well as homogeneous layers. The excitation is admitted for the full angular spectrum instead of plane wave excitation. In addition, backside excitation (s_-^b) is enabled in order to keep the symmetry. Usually, it is set to zero.

The Rayleigh modes are connected to the transversal field components via:

$$\begin{pmatrix} E_y \\ H_x \end{pmatrix} = \begin{pmatrix} 1 & 1 \\ \alpha & -\alpha \end{pmatrix} \cdot \begin{pmatrix} s_+ \\ s_- \end{pmatrix} \quad (6.1)$$

for TE-polarization and

$$\begin{pmatrix} H_y \\ E_x \end{pmatrix} = \begin{pmatrix} 1 & 1 \\ -\alpha/\varepsilon & \alpha/\varepsilon \end{pmatrix} \cdot \begin{pmatrix} s_+ \\ s_- \end{pmatrix} \quad (6.2)$$

for TM-polarization. The wave vector component α_m in the normal direction is obtained from β_m by means of the dispersion relation (with the normalization $\omega/c = 1$):

$$\varepsilon - \beta_m^2 = \alpha_m^2; \quad \Im(\alpha_m) \geq 0 \quad (7)$$

The two solutions of the quadratic equation give rise to waves propagating in the $\pm z$ direction. A detailed description of the RCWA can be found for example in ¹⁰ and ¹¹.

2.3 Application to SIL modeling

The algorithm developed in the previous section can be applied to the modeling of SIL scanning microscopy. We assume that the incident angular spectrum in the superstrate, i.e., within the SIL, is known. In case of aberration-free coupling optics it is simply a cone of rays within a certain numerical aperture. Then, the scatterer is sliced according to the RCWA-requirements and the diffraction matrix is computed (either r^f or t^f since the incidence is only from the front side). In order to perform a scan, the focussed spot has to be shifted across the specimen. This lateral shift x_0 as well as a defocusing z_0 of the probing beam can be expressed by additional phase terms applied to the incident angular spectrum $\tilde{A}_{m,0}$:

$$\tilde{A}_m = \tilde{A}_{m,0} \cdot \exp\left(i \frac{2\pi}{\lambda} \beta_m x_0\right) \cdot \exp\left(-i \frac{2\pi}{\lambda} \alpha_m z_0\right) \quad (8)$$

Once, the diffraction matrix of the problem is known, the detected intensity for all scan positions can be calculated by means of formula (3). This approach reduces the computation time drastically compared to FDTD and MMP methods.

3. CONFIGURATION, RESULTS AND DISCUSSION

In our model system, a SIL and a substrate, both with refractive index 2.2, are separated by an air gap of thickness h . The maximum incident angle θ_{\max} was set to $\sin \theta_{\max} = 0.9$ ($\theta_{\max} = 64.16^\circ$) and the illumination wavelength was taken to be $\lambda = 633$ nm. Generally, the illuminating wave came to a focus at the bottom surface of the SIL, i.e., the vertical coordinate in z_0 in equation (8) was set to zero.

The refractive index of the SIL defines the critical angle $\theta_c = 27.04^\circ$ ($1/n_{\text{SIL}} = \sin \theta_c$). Generally, when the air gap is large ($h \gg \lambda$), total internal reflection occurs at the bottom surface of the SIL for all incident angles $\theta > \theta_c$. The evanescent field which is created in the air gap will interact with the sample only when $h \ll \lambda$. The large angles which correspond to the high spatial frequencies and small sample structures are essential for high resolution imaging.

Two-point resolution is traditionally used as a measure of the resolving power of an optical system. In data storage applications, we consider two rectangular bits rather than two point sources. The bits are either deposited on top of the substrate or embedded in the surface (see fig. 2, sample a). They have a lateral extension of $L = 100$ nm, a height $l = 10$ nm and are separated by a distance of $S = 100$ nm.

These sample dimensions correspond to the Rayleigh criterion for resolution ($\delta = 0.61 \lambda / (n_{\text{SIL}} \text{NA}_{\text{air}}) \Rightarrow \delta = 195$ nm; with δ is the minimum resolvable distance). The bits are composed of either a metal (chromium) with refractive index $n_{\text{Cr}} = 3.5 + i 4.5$, or a dielectric material with $n_{\text{die}} = 2.2$ (see fig. 2). In this example the application of the RCWA needs two slices, one being the air gap (homogeneous slice) and one being a slice including the Cr or dielectric pattern. Both slices are sandwiched between superstrate and substrate.

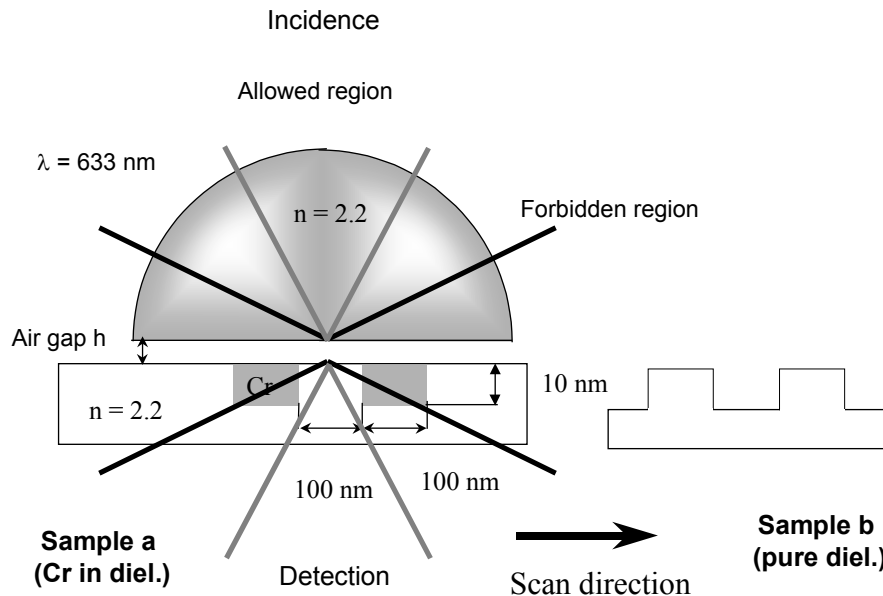


Fig.2: Schematic diagram of the experimental setup. The focus spot is located at the bottom surface of the SIL (hemisphere). SIL and sample are separated by an air gap (h). The sample a) consists of a double line of embedded Chromium bits in a dielectric with $n = 2.2$ and sample b) is a patterned dielectric. In both, SIL body and sample substrate we distinguish between “allowed-” and “forbidden-” excitation and detection range.

In the first simulation we studied the detection signal dependence on the illumination and imaging geometry. A sample with Cr bits embedded in the substrate was chosen. The air gap is set to zero. Fig. 3 shows the transmission efficiency as a function of the lateral focus position in TE – polarization for five different excitation and detection configurations (As common, the efficiency relates the total detected intensity to the incident intensity). The bits are centered at $x=0$ and $x=-0.2\text{ }\mu\text{m}$.

In both the illumination and detection geometry we distinguish between the inner cone and the outer ring which are separated by the critical angle θ_c . Following Hecht et al.¹² we consider the outer ring to be the “forbidden” region and consider the cone to be the “allowed” region (compare fig. 2).

The first curve (solid line) in fig. 3 shows the detection efficiency when both illumination and imaging are carried out over the full angle range ($0 < \sin \theta < 0.9$). Note that the radiation scattered into angles $\theta > \theta_c$ would be totally reflected at the bottom face of a plane parallel substrate. The detection of this part of the transmitted radiation requires a substrate with curved bottom surface such as a half sphere.

Approximately one micron away from the Cr bits, the detection efficiency is 100 %. This is expected because at this lateral position the SIL material and substrate form a homogeneous structure ($h = 0\text{ nm}$) and the incident light is directly transferred to the corresponding detection region. When the focus is scanned over the chromium bits the transmission efficiency is reduced to about 50 % due to reflection and absorption. In the center between the chromium bits a local maximum of 65 % in the efficiency curve occurs.

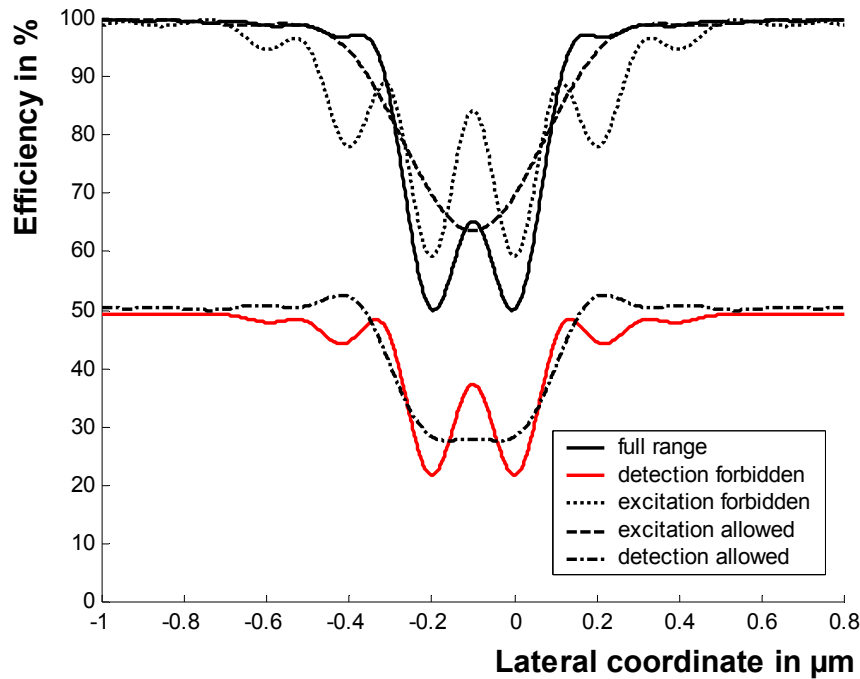


Fig.3: Transmitted efficiency as a function of the lateral scan position for different excitation and detection configurations. The sample consists of two separated ($S = 100$ nm) chromium bits with a lateral extension of $L = 100$ nm and a height $l = 10$ nm embedded in a dielectric material ($n = 2.2$) (see figure 1, sample a).

In the following, we denote the efficiency value that is obtained by scanning over an unpatterned sample, i.e., the scanning spot is far away from the patterned bits, as offset efficiency η_{off} . In terms of image processing, the signal is offset compensated by this back ground signal. The absolute value of η_{off} depends of course on the air gap. For the further discussion and evaluation of the resolution we define the modulation depth V :

$$V = \left| \frac{\eta_{\text{bit}} - \eta_{\text{inter}}}{\eta_{\text{bit}} - \eta_{\text{off}}} \right| \cdot 100\% \quad (9)$$

Here, η_{bit} describes the efficiency detected during probing the center of a bit and η_{inter} relates to the notch efficiency in the middle between the two bits. The classical Rayleigh limit corresponds to $V = 27\%$.

Using this definition we found a modulation depth of $V = 30\%$ for the first discussed configuration, which is comparable to the classical Rayleigh criterion.

The second curve (dashed) in fig. 3 shows the situation when the excitation is restricted to the allowed region and the detection is done over the full angle. The detection efficiency far away from the chromium structure is again 100 %. The curve clearly shows only one local minimum so that the bits are not resolved.

The following curve (dash-dotted) shows the result when the detection is limited to the allowed range and the excitation is done over the full range. Due to the limitation of the detection range, the baseline efficiency is reduced ($\sim 50\%$). The curve shows only a very small local maximum between the two chromium bits so that these two structures are just barely resolved.

When exciting in the forbidden range and detecting in the full range (dotted curve), again the baseline offset shows 100 % efficiency. Compared to the peak efficiency over the bit center, the local notch between the bits is

very prominent. For the modulation depth we found $V = 63\%$ which is much better than the classical Rayleigh limit. Although this setup offers an excellent modulation depth it also suffers under the remarkable sidelobes which also occur in far-field microscopy with annular illumination.

The last curve in fig. 3 (light solid) shows the situation when the excitation is done over the full range but the detection is limited to the forbidden range. Here the curve shows the two bits well resolved. For the modulation depth we found $V = 42\%$, which is also much better than the classical Rayleigh criterion. Since the sidelobes are also reduced in this configuration, it seems to be the best choice for signal analysis.

In the following, the scanning process over the embedded chromium bits is simulated in transmission (TE-polarization) for different air gap heights between the SIL and the sample. Due to the previous discussion, here the excitation is done over the full range, but the detection is limited to the forbidden range.

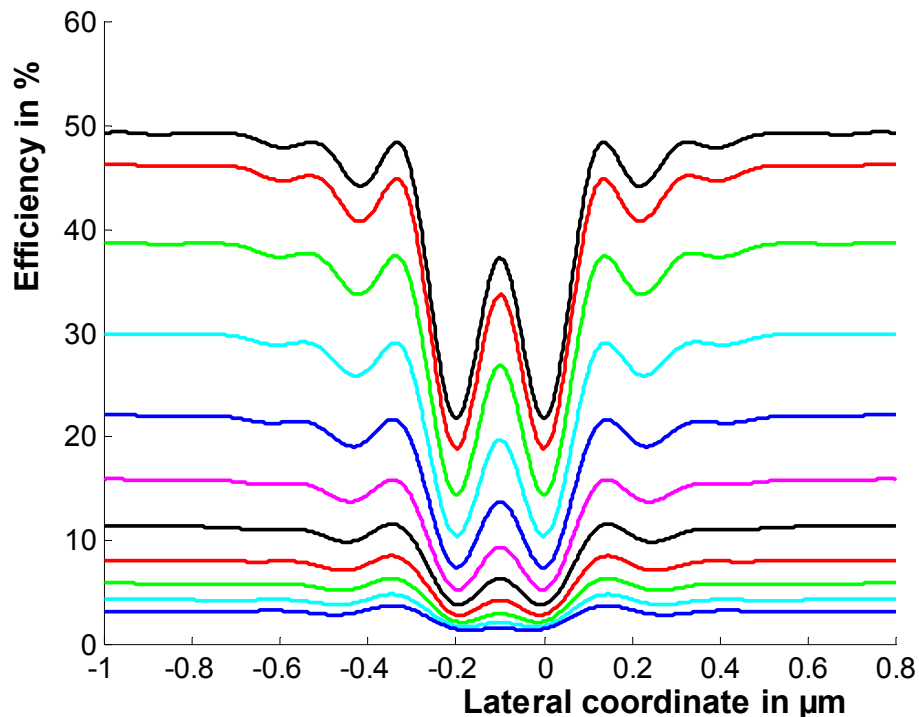


Fig. 4: Transmitted efficiency (sample a) vs lateral scan position for different air gaps (top curve: $h = 0$ nm, bottom curve $h = 200$ nm, step width 20 nm). The illumination cone comprises the full range ($\sin \theta = 0.9$), whereas the detection is reduced to the forbidden range (annulus from $\sin \theta = 0.45$ thru $\sin \theta = 0.9$).

In the next diagram (fig. 4), the dependency of the detection efficiency versus the lateral focus position for the different air gaps is depicted. The change of the baseline offset with the gap height is partially due to interference between SIL surface and upper substrate. Besides, it is also due to the decay of the evanescent field below the bottom SIL surface. This reduces the coupling efficiency from the forbidden range of the illumination to the substrate and thus degrades the resolution.

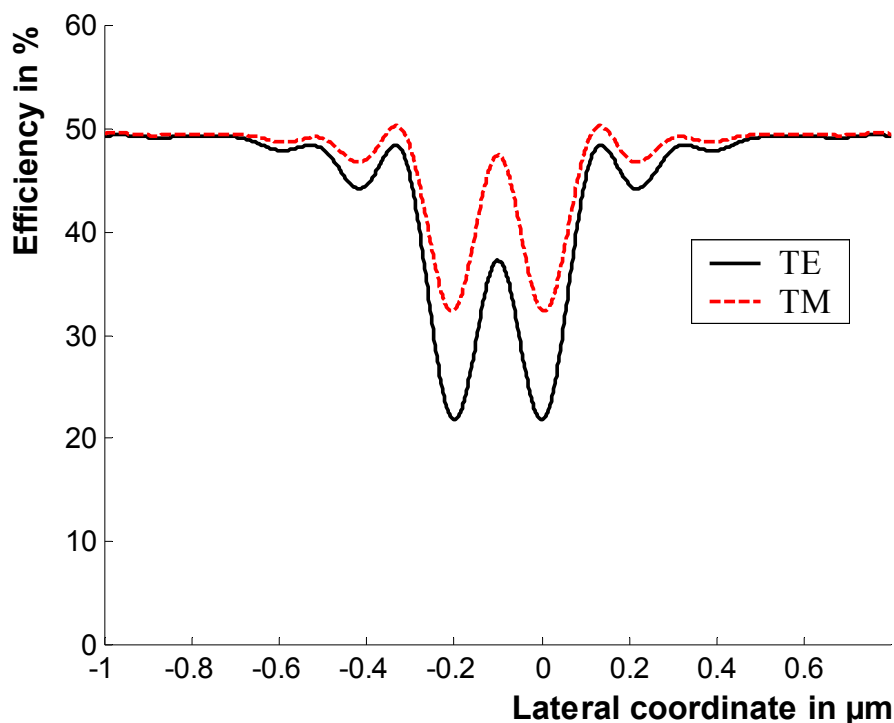


Fig. 5: Comparison of the transmitted efficiency (sample a) vs lateral scan position for TE- and TM-polarization ($h = 0$ nm) (excitation in the full range, detection reduced to the forbidden range).

With TM-polarization, the resolution also decreases with increasing separation, h . It is remarkable that the depth modulation for equivalent gap width is stronger in TM-polarization compared to the TE-polarization. The evaluation of both curves show that the Rayleigh limit ($V = 27\%$) is reached by air gaps of 75 nm in TM-polarization and 30 nm in TE-polarization respectively. The differences between TM- and TE-polarization can be associated to the boundary conditions on the surface of the chromium bits. For TM-polarization, the electrical field remains finite at the metallic boundaries and penetrates into the metallic structure so that the effective line width is reduced and the effective space width is enlarged. This influences the reduced absorption and reflection when the focus spot is located over the bits and an increased transmission efficiency when focussing on the lateral position between the bits. For TE-polarization the electrical field nearly vanishes at the chromium surface. Therefore the effective line- and space width acts vice versa compared to the TM-polarization and the modulation depth is less prominent.

The detection efficiency versus lateral position in reflection mode is shown in fig. 6. Due to energy conservation, the baseline offsets show the opposite dependence on gap distance, compared to transmission mode. The resolution is equivalent to the transmission mode.

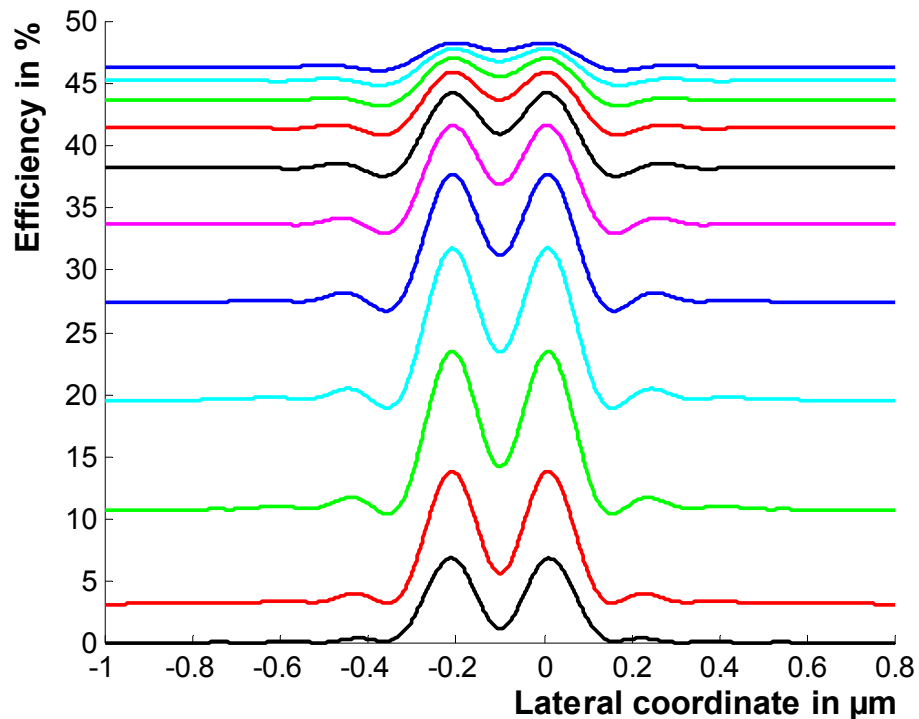


Fig. 6: Reflected efficiency vs lateral scan position for sample a). The different curves represent different air gaps (h). Excitation is done over the full range, detection is reduced to the forbidden range. (bottom curve: $h = 0$ nm, top curve $h = 200$ nm, step width 20 nm)

In the next example, we examine a structure where the Cr bits are replaced by dielectric bits ($n = 2.2$) of the same dimension but now deposited on top of the substrate (fig. 2, sample b). In this case, $h = 0$ means that the SIL is in contact with the bits. Fig. 7 exhibits the detection efficiency versus the lateral spot position. The baseline offsets show the same behavior as in fig. 6. Compared to the example with Cr bits, now the transmission efficiency is inverted. This inversion can be related to the smaller distance of the dielectric bits to the SIL, which disturbs the evanescent fields and results in an increased coupling efficiency into the substrate material. Moreover, the modulation for $h = 0$ is weaker than that for $h = 20$ or 40 nm. This is caused by the nonlinearity of the offset efficiency η_{off} versus air gap (smaller slope for $h = 0$ nm).

Essential in these curves is the reduced ratio of peak intensity to baseline offset. When normalizing the peak intensity over the bits and central dip to the baseline offset, the contrast seems to be very high. But in a real experiment, this advantage would be outweighed by the fact that a slight change in gap distance may disrupt the imaging and create a bit error.

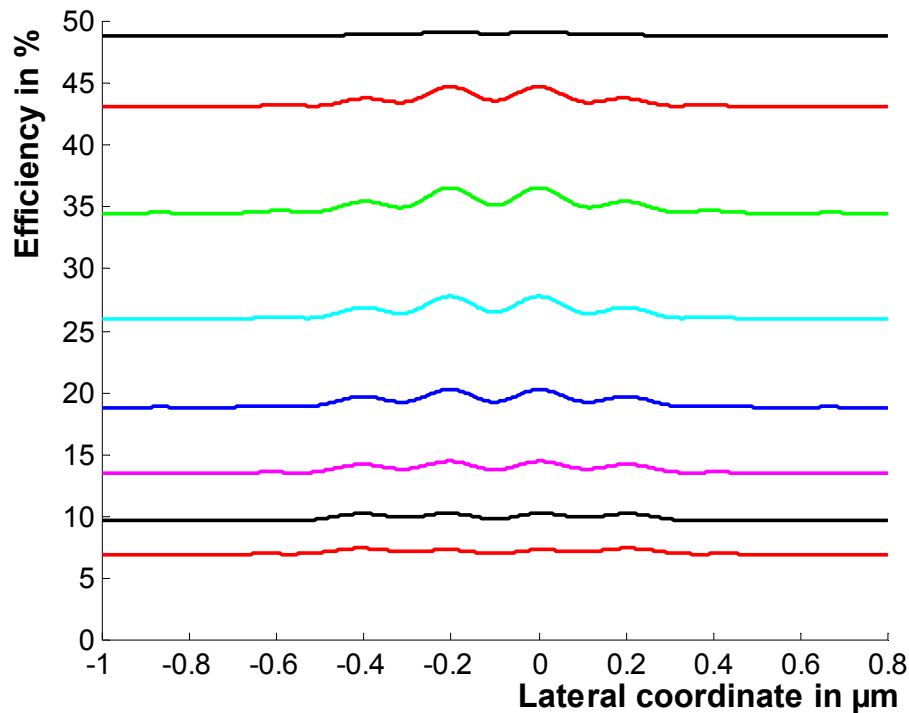


Fig. 7 Transmitted efficiency vs lateral scan position for a patterned dielectric sample (sample b in fig. 2). Top curve: $h = 0$ nm, bottom curve $h = 140$ nm, step width 20 nm. (excitation in the full range, detection reduced to the forbidden range)

4. CONCLUSION

An efficient rigorous method for the modeling of solid immersion microscopy was presented. The method is particularly appealing for the numerical exploration of scanning SIL on patterned samples. It is neither restricted to a reflection or transmission regime nor to periodic patterned samples. The preliminary results obtained from the simulations are consistent. They confirm the expected superresolution power of SIL. Particularly, it has been shown that a 100 nm separated double line (linewidth 100 nm) can be clearly resolved with 633 nm probing wavelength. However, due to the decay of the evanescent waves, the air gap has to be kept both as small as possible and very stable. Distinct differences between absorbing and pure phase patterns have been observed. While chromium patterns gave a strong signal, the signal modulation from dielectric samples is weak. First numerical investigations hint that more sophisticated detection units could improve the situation.

ACKNOWLEDGEMENT

This work was financially supported by the German Ministry of Science (BMBF) with the responsibility of the Deutsche Forschungsanstalt für Luft- und Raumfahrt e.V. (DLR) under Grant No. 01 BS 608/9. We thank Prof. Karl Hehl for invaluable discussion and advice.

REFERENCES

1. S. M. Mansfield, G. S. Kino, "Solid immersion microscope," *Appl. Phys. Lett.* **57** (24) pp. 2615-2616, 1990.
2. G. S. Kino, "The solid immersion lens," *Proc. SPIE Vol.* **3740**, pp. 2-5, 1999.
3. G. S. Kino, "Applications and theory of the solid immersion lens," *Proc. SPIE Vol.* **3609**, pp. 56-66, 1999.
4. Feng Guo, T. E. Schlesinger and D. D. Stancil, "Optical field study of near-field optical recording with a solid immersion lens," *Appl. Opt.* **39**, pp. 324-332, 2000.
5. I. Ichimura, K. Osato, F. Maeda, H. Owa, H. Ooki, G. S. Kino, "High Density Optical Disk System Using a Solid Immersion Lens," *Proc. SPIE Vol.* **2514**, pp. 176-181, 1995.
6. T. D. Milster, J. S. Jo, K. Hirota, "Roles of propagating and evanescent waves in solid immersion lens systems," *Appl. Opt.* **38**, pp. 5046-5057, 1999.
7. Wei-Hung Yeh, Lifeng Li, and M. Mansuripur, "Vector diffraction and polarization effects in an optical disk system," *Appl. Opt.* **37**, pp. 6983-6988, 1998.
8. A. K. Wong and A. R. Neureuther, "Massively parallel electromagnetic simulation for photolithography applications," *IEEE Transactions on CAD* **14**, pp. 1231-1240, 1995.
9. L. Novotny, D. W. Pohl, and P. Regli, "Light propagation through nanometer-sized structures: the two-dimensional-aperture scanning near-field optical microscope," *J. Opt. Soc. Am.* **A 11**, pp. 1768-1779, 1995.
10. Lifeng Li, "Multilayer modal method for diffraction gratings of arbitrary profile, depth, and permittivity," *J. Opt. Soc. Am.* **A 10**, pp. 2581-2591, 1995.
11. M. G. Moharam, D. A. Pommet, E. B. Grann, and T. K. Gaylord, "Stable implementation of the rigorous coupled-wave analysis for surface-relief gratings: enhanced transmittance matrix approach," *J. Opt. Soc. Am.* **A 12**, pp. 1077-1086, 1995.
12. B. Hecht, H. Heinzelmann, and D.W. Pohl, "Combined aperture SNOM/PSTM: best of both worlds?" *Ultramicroscopy* **57**, pp. 228-234, 1995.

*Correspondence: Email: j.bischoff@zeiss.de; Telephone: +493641 64 2850